Journal of Remote Sensing
A SCIENCE PARTNER JOURNAL

RESEARCH ARTICLE

Satellite-Observed Increase in Aboveground Carbon over Southwest China during 2013-2021

Lei Fan[1,2], Guanyu Dong[1,2*], Frédéric Frappart[3,4], Jean-Pierre Wigneron[3,4], Yuemin Yue[5], Xiangming Xiao[6], Yao Zhang[7], Shengli Tao[8], Lin Cao[9], Yuechen Li[1,2], Mingguo Ma[1,2], Hongqian Fang[1,2], Ling Yu[1,2], Zanpin Xing[10], Xiaojun Li[3,4], Weiyu Shi[1,2], Xiuzhi Chen[11], and Rasmus Fensholt[12]

[1]Chongqing Jinfo Mountain Karst Ecosystem National Observation and Research Station, School of Geographical Sciences, Southwest University, Chongqing 400715, China. [2]Chongqing Engineering Research Center for Remote Sensing Big Data Application, School of Geographical Sciences, Southwest University, Chongqing 400715, China. [3]Université de Bordeaux, 33400 Talence, France. [4]INRAE, Bordeaux Sciences Agro, UMR 1391 ISPA, 33140 Villenave-d'Ornon, France. [5]Key Laboratory for Agro-ecological Processes in Subtropical Region, Institute of Subtropical Agriculture, Chinese Academy of Sciences, Changsha, China. [6]Department of Microbiology and Plant Biology, Center for Earth Observation and Modeling, University of Oklahoma, Norman, OK 73019, USA. [7]Sino-French Institute for Earth System Science, College of Urban and Environmental Sciences, Peking University, Beijing 100101, China. [8]Institute of Ecology, College of Urban and Environmental Sciences, Peking University, Beijing 100871, China. [9]Co-Innovation Center for the Sustainable Forestry in Southern China, Nanjing Forestry University, Nanjing 210037, China. [10]Cryosphere Research Station on the Qinghai-Tibet Plateau, State Key Laboratory of Cryospheric Science, Northwest Institute of Eco-Environment and Resource, Chinese Academy of Sciences, Lanzhou, Gansu 730000, China. [11]School of Atmospheric Sciences, Sun Yat-sen University, Zhuhai 519082, Guangdong, China. [12]Department of Geosciences and Natural Resource Management, University of Copenhagen, Copenhagen, Denmark.

*Address correspondence to: dgy199909@email.swu.edu.cn

Over the past 4 decades, Southwest China has the fast vegetation growth and aboveground biomass carbon (AGC) accumulation, largely attributed to the active implementation of ecological projects. However, Southwest China has been threatened by frequent extreme drought events recently, potentially countering the expected large AGC increase caused by the ecological projects. Here, we used the L-band vegetation optical depth to quantify the AGC dynamics over Southwest China during the period 2013-2021. Our results showed a net AGC sink of 0.064 [0.057, 0.077] Pg C year^{-1} (the range represents the maximum and minimum AGC values), suggesting that Southwest China acted as an AGC sink over the study period. Note that the AGC loss of 0.113 [0.101, 0.136] Pg C year^{-1} was found during 2013-2014, which could mainly be attributed to the negative influence of extreme droughts on AGC changes in Southwest China, particularly in the Yunnan province. For each land use type (i.e., dense forests, persistent forests, nonforests, afforestation, and forestry), the largest AGC stock increase of 0.032 [0.028, 0.036] Pg C year^{-1} was found in nonforests, owing to their widespread land cover rate over Southwest China. For AGC density (i.e., AGC per unit area), the afforestation areas showed the largest AGC density increase of 0.808 [0.724, 0.985] Mg C ha^{-1} year^{-1}, reflecting the positive effect of afforestation on AGC increase. Moreover, the karst areas exhibited a higher increasing rate of AGC density than nonkarst areas, suggesting that the karst ecosystems have a high carbon sink capacity over Southwest China.

Citation: Fan L, Dong G, Frappart F, Wigneron JP, Yue Y, Xiao X, Zhang Y, Tao S, Cao L, Li Y, et al. Satellite-Observed Increase in Aboveground Carbon over Southwest China during 2013-2021. *J. Remote Sens.* 2024;4:Article 0113. https://doi.org/10.34133/remotesensing.0113

Submitted 12 June 2023
Accepted 10 January 2024
Published 7 February 2024

Introduction

Over the past 4 decades, Southwest China has acted as the predominant carbon sink [1–4], absorbing a huge amount of anthropogenic CO_2 [3]. Yet, Southwest China was threatened by frequent occurrences of extreme droughts in recent 2 decades (e.g., in the years 2009-2013 and 2022), resulting in a large reduction in vegetation greenness [5], gross primary productivity [6], and aboveground biomass carbon (AGC) [3]. These drought events (e.g., 2009/2010 winter–spring drought, 2011 and 2013 summer droughts) have decreased the AGC sink over Southwest China or even flipped the AGC sink into an AGC loss [7]. For

example, a carbon loss caused by drought was observed over Southwest China, using satellite and ground observations [7–10]. These results are opposite to the net carbon sink over Southwest China reported by some prior studies [1,3,4,11,12], partly due to the divergent study periods and methods for estimating the carbon sinks of Southwest China. Hence, it is necessary to further quantify the AGC budget over the Southwest China.

In addition, the karst regions, accounting for about one-third of the Southwest China, have the fragile geological environment characterized by excessive human disturbances, soil erosion, land and vegetation degradation, and rock desertification during the past century [13]. These issues made the carbon sink of karst ecosystems to be more vulnerable to climate change [14] than other landscapes. Meanwhile, frequent anthropogenic disturbances have led to a large reduction in vegetation cover [11], leading to the AGC loss over the Southwest China karst [15,16]. Since 1999, a succession of ecological projects were carried out under the support of the Chinese government, in order to convert croplands and degraded lands into forests, as well as protect existing forests and decrease rocky desertification [17]. Such projects include the Natural Forest Protection Project, the Grain to Green Project, the Zhujiang River Shelter Forest Project, and the Karst Rocky Desertification Restoration Project [18–20].

These intensive ecological restoration projects above could largely compensate for the AGC reductions caused by natural and human disturbances [21,22], especially for the Southwest China karst areas. The ecological projects can also result in a change of land use type [12], such as the transition from nonforests to forests, through the implementation of land management policies (e.g., forest protection and tree planting). To date, the karst areas are mainly covered by forests and shrublands enhancing the carbon sink capacity of the karst ecosystem, contrary to the prior state characterized by degraded lands and croplands [21]. However, it is unclear whether the magnitude of AGC sink per unit area (i.e., AGC density) in karst areas is higher than in nonkarst areas, although the karst areas smaller than nonkarst areas. Thus, the contribution of ecological projects to the increase in AGC density over Southwest China should be assessed.

Previous studies [23–25] monitored the temporal dynamics of AGC mainly using optical vegetation indices (VIs) like gross primary productivity and leaf area index (LAI), which are characterized by a long-time span and relatively high spatial and temporal resolutions [26,27]. However, the accuracy of optical VIs is known to be influenced by cloud contamination, forest canopy structure, and topography [27]. Affected by the East Asian monsoon, frequent precipitation and cloudy conditions resulted in an average sunshine duration of only 2,175 hours year^{-1} over Southwest China, which is lower than the national average level of 2,430 hours year^{-1} [28]. The rainy season in Southwest China could reduce the data quality of Moderate Resolution Imaging Spectroradiometer (MODIS) LAI, resulting in more than 25% of bad-quality observations during the summer period [29]. Furthermore, optical VIs could be affected by saturation issues in densely vegetated areas and are only indirectly sensitive, through the photosynthetic activity of the leaves, to trunk and branch biomass [30,31], causing potential uncertainties in AGC estimation over Southwest China.

The L-band vegetation optical depth (L-VOD) has been widely used to quantify the AGC budgets over the China [4], Africa [32], Siberia [33], Amazon [34], and the pan-tropics [35,36]. In contrast to VOD products obtained from high-frequency bands (such as C, X, Ku bands, 6.9 to 18.7 GHz) [37], low-frequency VOD (L band, 1.4 GHz) is more sensitive to the overall vegetation structure (encompassing vegetation canopy and stem) and is more related to the biomass spatial distributions [31,38]. Moreover, L-VOD is hardly impacted by atmospheric conditions and the presence of clouds [37]. Thus, L-VOD is highly suitable for monitoring the large-scale spatial and temporal AGC dynamics over Southwest China.

The major aims of the present study are: (a) to examine spatial-temporal patterns of the L-VOD-derived AGC over Southwest China during 2013-2021; (b) to evaluate the impact of ecological projects on AGC changes over Southwest China; and (c) to assess the carbon sink capacity of karst areas over Southwest China.

Materials and Methods

Study area

Southwest China (20°54′N to 34°19′N, 96°21′E to 112°04′E) consists of Sichuan, Yunnan, Guizhou, Chongqing, and Guangxi provinces (Fig. 1). The elevation gradually increases from the southeastern to the northwestern parts of the region [39]. Average yearly precipitation ranged from 1,000 to 1,300 mm. The dominant vegetation types over Southwest China are forests (widely distributed in the Hengduan Mountains, western Yunnan, northern Guangxi, and eastern Guizhou), croplands (widely distributed in the Sichuan Basin and southern Guangxi), shrublands (widely distributed in the Yunnan-Guizhou Plateau), and grasslands (widely distributed in the northwestern Sichuan) [40]. Moreover, Southwest China has 0.55 million km^2 of karst landscapes [41], which are located in the Yunnan-Guizhou Plateau, eastern Chongqing, and northern Guangxi.

Datasets

Land use map and karst map

The 500-m land use map provided by Tong et al. [12] (hereafter referred to as Tong map) was used to get information about the land use change and to explore the effect of ecological projects on AGC changes over Southwest China. The Tong map was based on a random forest (RF) model, driven by MODIS MCD43A4 reflectance, GF-1 satellite images, and tree cover

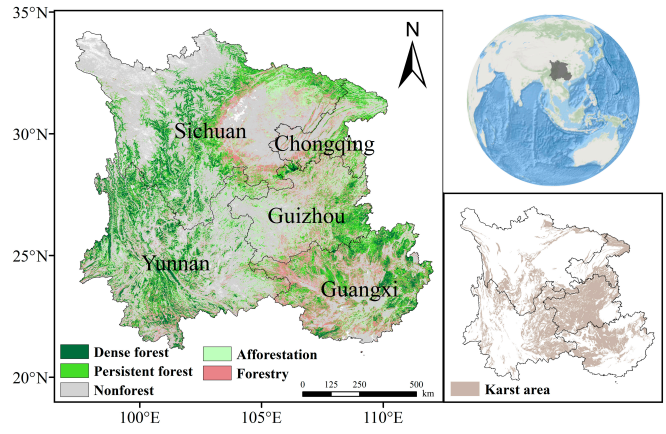

Fig. 1. The geographical location of Southwest China, the spatial distribution of karst areas, as well as the land use map over Southwest China. The land use types of Southwest China are separated into 5 classes, including "Dense forest", "Forest", "Nonforest", "Afforestation", and "Forestry". The land use map is provided by Tong et al. [12].

datasets, covering the period of 2002-2017. The original Tong map contains 8 land use types, including "Dense forest", "Forest", "Nonforest", "Recovery", "Afforestation", "Deforestation", "Rotation" and "Rotation$_L$" (defined by the areas with harvesting by large-scale forestry), which were further merged into 5 land use types in this study:

1. "Dense forest" (refer to "Dense forest" of Tong map [12]) contains protected remnant forests and secondary forests characterized by a dense forest canopy. According to the description of Tong map [12], all pixels classified as the "Dense forest" type were defined as forest areas characterized by frequent anthropogenic protection within ecological projects.

2. "Persistent forest" (refer to "Forest" of Tong map [12]) represents the less dense forests without human disturbances, namely, no substantial harvesting activities occurred in this type. According to the description of Tong map [12], all pixels classified as the "Persistent forest" type were defined as anthropogenic semimanaged forest areas within ecological projects.

3. "Nonforest" (refer to "Nonforest" of Tong map [12]) mainly includes shrubs grasslands and croplands and also incorporates fruit trees and small patches of trees. According to the description of Tong map [12], all pixels classified as the "Nonforest" type were defined as persistent nonforest areas under anthropogenic management within ecological projects.

4. "Afforestation" (by merging the "Recovery" and "Afforestation" types of the Tong map [12]) contains areas with natural forest recovery and tree plantations, indicating the land use change from nonforests to forests. According to the description of Tong map [12], all pixels classified as the "Afforestation" type were defined as the afforested areas within ecological projects.

5. "Forestry" (by merging the "Deforestation", "Rotation", and "Rotation$_L$" of the Tong map [12]) represents extensive timber harvesting affected by forestry, consisting mainly of clear-cutting of forest stands and following regeneration (thus exhibiting dynamic land use change between forests and nonforests). According to the description of Tong map [12], all pixels classified as the "Forestry" type did not belong to the ecological project implementation areas.

In these land use types above, all pixels classified as "Dense forest", "Persistent forest", "Nonforest", and "Afforestation" types belonged to the ecological project implementation areas (Fig. 1). To explore the interannual variation of AGC in the karst areas, a karst map was selected (Fig. 1). Here, the land use map and karst map were aggregated to 0.25° resolution using a majority rule (Fig. S1).

L-VOD

The estimations of AGC were derived from L-VOD based on the Soil Moisture and Ocean Salinity INRA-CESBIO (SMOS-IC) V2 algorithm [42]. The SMOS-IC V2 product offers daily L-VOD at a spatial resolution of 0.25° from both ascending and descending orbits during 2010-2021, which could exhibit a good relationship with AGC [42]. Therefore, the SMOS-IC L-VOD has been broadly used to assess the spatial distribution of AGC [32,35,36].

Because L-VOD data is disturbed by the radio frequency interference (RFI) in China [43], we used a strict filtering method to select good-quality VOD data. The root mean square error (RMSE) between the measured and simulated brightness temperature (TB-RMSE) linked to the SMOS-IC L-VOD product was selected as a factor to remove the pixels impacted by strong RFI [42]. The filtering method comprises the following steps:

1. Daily L-VOD data with scene flag (SF) > 3 and TB-RMSE > 8 k were removed [35], with SF > 3 corresponding to pixels with complex topography.

2. We further calculated the remaining L-VOD data from ascending (i.e., L-VOD$_{ASC}$) and descending (i.e., L-VOD$_{DESC}$) orbits for each trimester (3-month period), respectively. If the difference between average L-VOD$_{ASC}$ and L-VOD$_{DESC}$ data was larger than 0.05 and the trimester average of the TB-RMSE from the ascending (or descending) orbit was larger than 7k, all the L-VOD$_{ASC}$ (or L-VOD$_{DESC}$) data within this trimester were removed.

3. Following step (2), we associated all the filtered L-VOD$_{ASC}$ and L-VOD$_{DESC}$ data in a combined data set (i.e., L-VOD$_{COM}$). Note that if the L-VOD$_{ASC}$ and L-VOD$_{DESC}$ data are available on the same day, we only keep L-VOD data with lower TB-RMSE.

4. For each trimester, we computed the standard deviation (SD) and mean value of L-VOD$_{COM}$ data, the daily L-VOD$_{COM}$ data falling outside of mean ± 2SD were removed. All the remaining L-VOD$_{COM}$ data were used to estimate the AGC changes.

MODIS LAI

LAI is associated with the vegetation greenness fractions and therefore potentially related to AGC [4]. The MODIS MOD15A2H V6 product offers an 8-d composite LAI at a 500-m resolution [44]. All good-quality pixels (according to the QC layers) of LAI during the period 2013-2021 were selected.

MODIS normalized difference vegetation index (NDVI)

The MOD13A2 V6.0 product provides a 16-d average NDVI at 1-km resolution [45], which is generated by averaging the best pixels available from all the observations within a 16-d period. All high-quality pixels (according to the QC layers) of NDVI over the study period were selected.

Meteorological data

Three meteorological data were selected to analyze the response of AGC to extreme droughts and the meteorological conditions over the Southwest China, including:

1. Precipitation, provided from Climate Hazards Group InfraRed Precipitation with Station data (CHIRPS) [46]. The CHIRPS offers global daily precipitation at 0.05° spatial resolution. A previous study [46] shows that the CHIRPS precipitation shows a good performance in drought monitoring. Daily CHIRPS precipitation data from 2013 to 2021 were used.

2. Soil moisture, obtained from the fifth-generation European Centre for Medium-Range Weather Forecasts reanalysis (ERA5) at 0.25° resolution [47]. Compared to precipitation, soil moisture after water distribution (through evapotranspiration and runoff) is considered as a variable more directly affecting vegetation growth over Southwest China [5,48]. In addition, root-zone soil moisture (RZSM) corresponds to the soil moisture content available for vegetation growth. The ERA5 soil column is divided into 4 soil layers (i.e., 0 to 7, 7 to 28, 28 to 100, and 100 to 289 cm). Here, monthly ERA5 soil moisture at the depths of 0 to 7 (θ_{7cm}), 7 to 28 (θ_{28cm}), and 28 to 100 (θ_{100cm}) was selected to compute RZSM using a weighted average method [49], as follows:

$$RZSM = 0.07 \times \theta_{7cm} + 0.21 \times \theta_{28cm} + 0.72 \times \theta_{100cm} \quad (1)$$

3. Standardized precipitation–evapotranspiration index (SPEI), provided from the global SPEI database [50]. SPEI is based on

multiple climatological factors from CRU TS 4.05, spanning the period during 1901-2020 [50]. Monthly SPEI at a resolution of 0.5° was averaged yearly to compute a yearly SPEI index; pixels that experienced yearly SPEI < -1 during 2009-2020 (which included the years of above mentioned extreme drought events in Southwest China) were defined as drought-affected pixels [51,52].

The above-mentioned vegetation proxies (i.e., L-VOD, LAI, and NDVI) and meteorological data (i.e., precipitation, SM, and SPEI) were aggregated to yearly values at 0.25° using the sample average method.

Topographic data

The 30-m topographic data was obtained from the Shuttle Radar Topography Mission [53]. Southwest China is predominantly mountainous terrain, which may affect the accuracy of AGC estimates. Thus, the elevation and relief amplitude were selected as indicators of topographic variation and complexity to assess the influence of topography on the estimations of AGC over Southwest China. The relief amplitude was calculated as the difference between the maximum and minimum elevation values within a 3×3 moving window [29]. The elevation and relief amplitude were aggregated to 0.25°resolution.

AGC benchmark map

Four AGC benchmark maps (Fig. S2) were selected to calibrate the relationship between AGC and L-VOD, as follows:

1. The Saatchi map [54] contains the AGC estimates at a 1-km spatial resolution circa 2015. It utilized GLAS LiDAR measurements to drive the comprehensive estimation of AGC, combining MODIS and QuickSCAT data. The Saatchi AGC map used here is an updated version derived from the Landsat, MODIS, Shuttle Radar Topography Mission, and Advanced Land Observing Satellite data.

2. The Baccini map [55] represents the AGC estimates at a 500-m spatial resolution circa 2007-2008. Compared to the Saatchi map, the Baccini map was produced using the GLAS and MODIS products based on the RF model.

3. The Saatchi-WT map [56], providing the AGC estimates at a 1-km resolution circa 2010. Using the weighting technique (WT) method, the Saatchi-WT map was generated by integrating 5 published AGC maps in forest areas [54,55,57–59] and the Saatchi map over nonforest areas. According to the description of the Saatchi-WT map, the forest and nonforest areas were identified utilizing the land cover map from Liu et al. [60].

4. The Su map [57] contains the forest AGC estimates at a 1-km resolution circa 2005. It was produced based on an RF model, using optical remote sensing data, GLAS LiDAR, and ground inventory measurements.

All 4 AGC benchmark maps (i.e., Saatchi map, Baccini map, Saatchi-WT map, and Su map) were aggregated to 0.25° resolution. In addition, the biomass density units (Mg ha^{-1}) of these maps were converted to the carbon density units (Mg C ha^{-1}) by multiplying AGC values by a factor of 0.5 [55].

Methods

AGC changes estimated using L-VOD

The annual AGC products using L-VOD were produced based on the same method as used by Fan et al. [35]: Firstly, the L-VOD data were sorted in ascending order and grouped into bins consisting of 250 grid pixels, and then the average L-VOD value for each bin was calculated. Subsequently, the mean AGC value from the corresponding distribution in the AGC benchmark maps (i.e., Saatchi map, Baacini map, Saatchi-WT map, and Su map) was computed for each L-VOD bin, thereby establishing the AGC curve as a function of L-VOD. This curve was fitted by a power regression equation [33]:

$$AGC_{ref} = a \times VOD^{b} \tag{2}$$

where a and b are parameters calibrated to obtain the best-fit curve. AGC_{ref} is the benchmark AGC, and VOD is the mean annual L-VOD value in 2015. For evaluating the uncertainties associated with AGC estimates calculated for each AGC benchmark map, we calculated the correlation coefficients (r) and RMSE between benchmark AGCs and bootstrapped AGC estimates using a bootstrap cross-validation method. In addition, the 95% bootstrap confidence interval of the AGC estimates retrieved from 4 AGC benchmark maps was calculated.

Given that the area of each land use type varies greatly, the dynamics of AGC density (i.e., AGC per unit area; Mg C ha^{-1}) values and AGC stock (Mg C) values for each land use type were analyzed. In comparison to the AGC stock changes, quantifying the AGC density changes can allow us to better analyze the effect of ecological projects on the increase of carbon sink of Southwest China. Similarly, the carbon sink capacity of karst areas was assessed by calculating the AGC density changes over the study period, because the karst area accounts for about 30% of Southwest China (Fig. 1). Accordingly, the time series of AGC density maps (Mg C ha^{-1}) during 2013-2021 were generated based on Eq. 2. The AGC stocks (Mg C) over Southwest China from 2013 to 2021 were computed by multiplying yearly AGC density by each pixel area. The net AGC changes (including AGC stock changes and AGC density changes) were computed by the difference in yearly values between 2013 and 2021. AGC gross gains and losses were computed, respectively, by aggregating positive and negative AGC changes over consecutive years spanning from 2013 to 2021.

We used the median values of 4 L-VOD retrieved AGC maps (i.e., $AGC_{Saatchi}$, $AGC_{Baccini}$, $AGC_{Saatchi\text{-}WT}$, and AGC_{Su}) to represent the AGC dynamics over Southwest China during 2013-2021. The maximum and minimum AGC values were also reported, because they could provide a comprehensive assessment of AGC dynamics and the uncertainty of retrieved AGC estimations.

Trend analysis

The interannual variation of annual vegetation proxies (i.e., AGC, NDVI, and LAI) and meteorological data (i.e., precipitation and RZSM) were calculated by a linear regression method, which is represented as follows:

$$Slope = \frac{\sum_{i=1}^{n}\left(year_i - \overline{year}\right) \times \left(Var_i - \overline{Var}\right)}{\sum_{i=1}^{n}\left(year_i - \overline{year}\right)^2} \tag{3}$$

where n is the number of study periods. Var_i is the annual variable value in year i. $Slope$ represents the trend of the temporal variations. We also selected the P value to identify the pixels with significant trends ($P < 0.1$) using an F test [61].

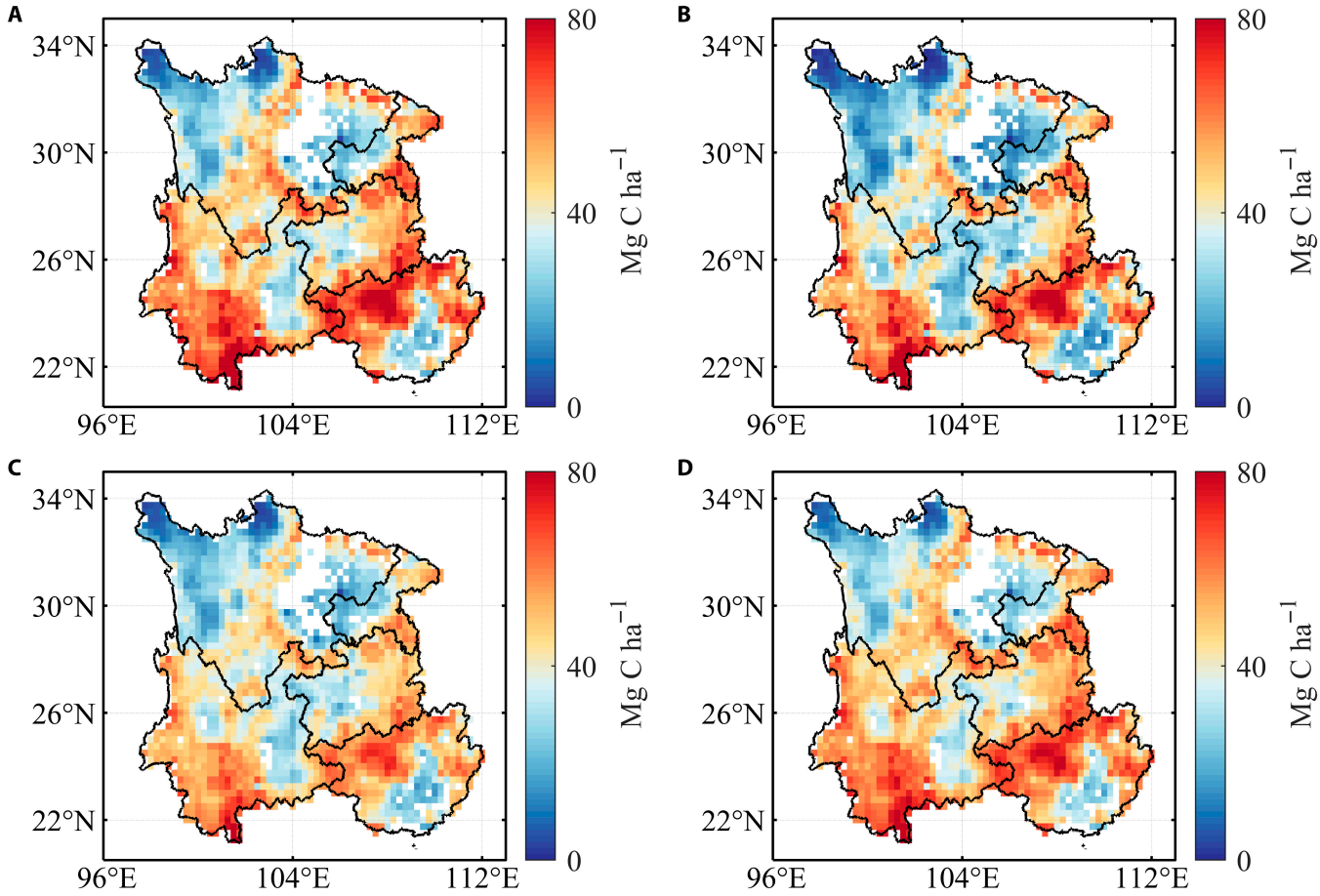

Fig. 2. Spatial patterns of 4 L-VOD derived AGC maps for the first year of study in 2013 over Southwest China. (A) $AGC_{Saatchi}$. (B) $AGC_{Baccini}$. (C) $AGC_{Saatchi\text{-}WT}$. (D) AGC_{Su}.

Results

Spatial pattern of AGC over Southwest China

The 4 L-VOD-derived AGC maps (i.e., $AGC_{Saatchi}$, $AGC_{Baccini}$, $AGC_{Saatchi\text{-}WT}$, and AGC_{Su}) in 2013 exhibited a similar spatial pattern of AGC density over Southwest China (Fig. 2). High AGC values were mainly located in the southern regions of study area (i.e., Southeastern Chongqing, eastern Guizhou, northern Guangxi, and southwestern Yunnan provinces). Low AGC values were observed in northwestern Sichuan and the Sichuan Basin (Fig. 2), which are dominated by grasslands and croplands, respectively.

In the year 2013, nonkarst areas showed the largest AGC stocks of 3.501 [3.239, 3.736] Pg C (the range represents the maximum and minimum AGC values calculated by 4 AGC benchmark maps) (Fig. 3A), accounting for 68.85% of the total AGC stocks over Southwest China. Meanwhile, the karst areas showed AGC stocks of 1.584 [1.476, 1.685] Pg C (Fig. 3A). For AGC density (indicated by the AGC per unit area), a higher AGC density was observed over the karst areas (45.167 [41.665, 48.176] Mg C ha^{-1}), relative to the nonkarst areas of 42.721 [39.573, 45.585] Mg C ha^{-1} (Fig. 3B). Among land use types, the largest AGC stocks were found in nonforests (2.767 [2.460, 2.992] Pg C) that covers the majority (62.55%) of the study area, followed by persistent forests (1.187 [1.092, 1.250] Pg C), forestry (0.483 [0.445, 0.509] Pg C), dense forests (0.377 [0.347, 0.397] Pg C), and afforestation (0.298 [0.275, 0.318] Pg C)

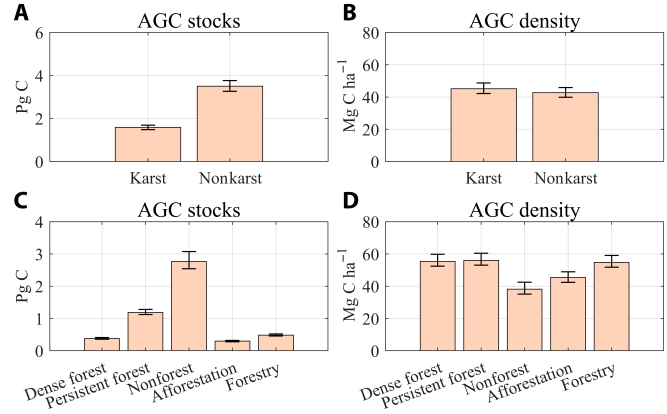

Fig. 3. AGC estimates for the first year of study in 2013. (A) AGC stocks and (B) AGC density over the karst and nonkarst areas. (C) AGC stocks and (D) AGC density for each land use type. The error bars represent the uncertainties of AGC stocks and AGC density estimated by 4 AGC benchmark maps.

(Fig. 3C). The highest AGC density was found in persistent forests (56.003 [51.550, 59.015] Mg C ha^{-1}), followed by dense forests (55.372 [50.916, 58.283] Mg C ha^{-1}), forestry (54.766 [50.452, 57.730] Mg C ha^{-1}), afforestation (45.410 [41.904, 48.420] Mg C ha^{-1}), and nonforests (38.203 [33.958, 41.302] Mg C ha^{-1}) (Fig. 3D).

AGC changes in space and time

The period of analysis contained several extreme drought events linked to the AGC losses, potentially introducing uncertainties in AGC trend analysis. Therefore, the analysis of our results was mainly based on the yearly net AGC changes. Our study revealed a gross AGC loss of −0.007 [−0.006, −0.009] Pg C year^{-1} was offset by a gross AGC gain of +0.071 [+0.063, +0.086] Pg C year^{-1} during 2013-2021, leading to a net sink of +0.064 [+0.057, +0.077] Pg C year^{-1} over Southwest China (Fig. 4A). Both LAI and NDVI showed an increasing trend over the study period (Figs. S3 and S4), which are in line with the AGC trends. At the provincial scale (Fig. 4B to F), the Sichuan province had the largest AGC sink of +0.026 [+0.024, +0.031] Pg C year^{-1}, followed by Guangxi (+0.013 [+0.012,

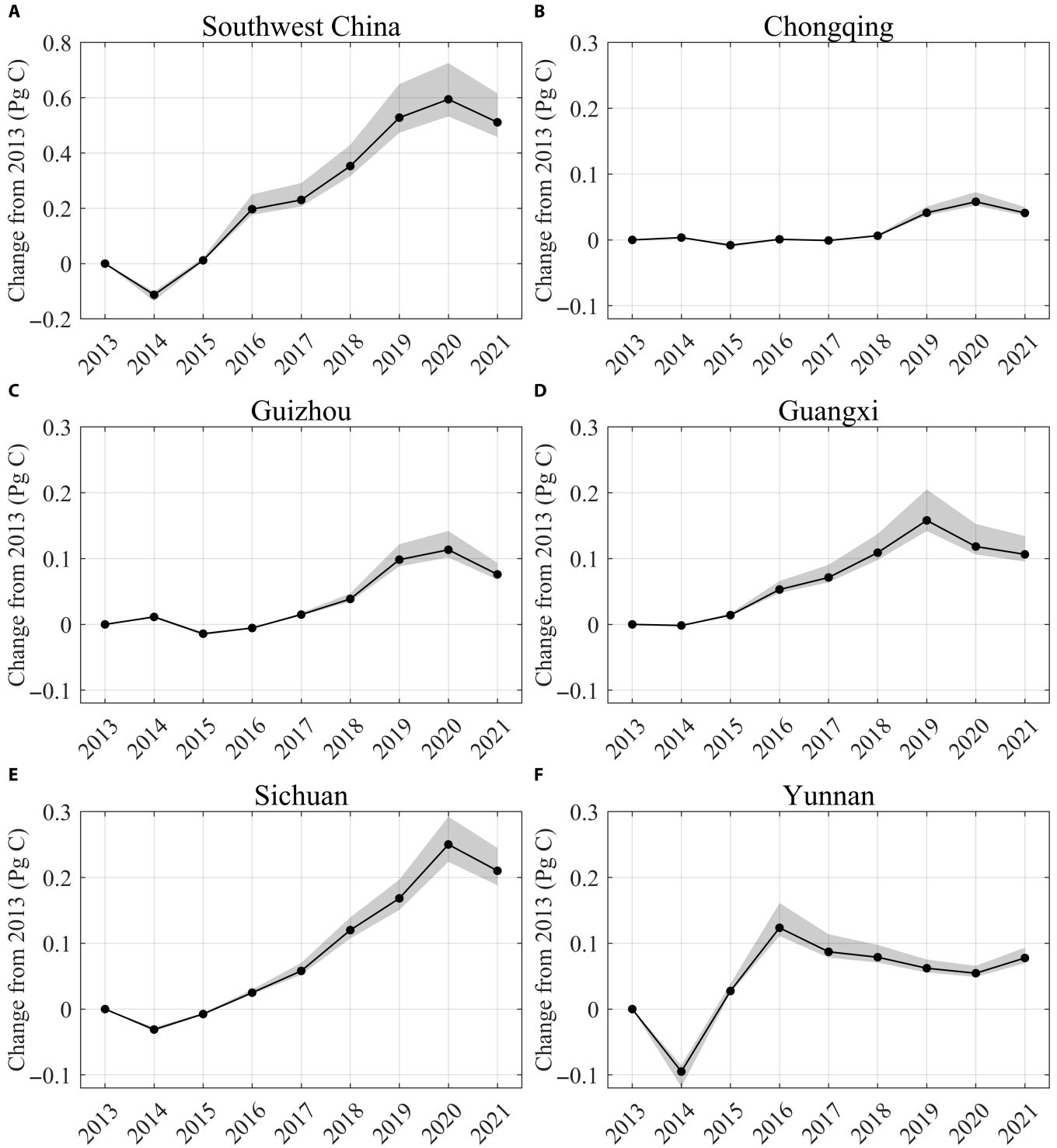

Fig. 4. Yearly net AGC changes from 2013 over Southwest China. The AGC values shown were subtracted from the 2013 baseline values. (A to F) Net AGC changes for the Southwest China, Chongqing, Guizhou, Guangxi, Sichuan, and Yunnan provinces, respectively. The shaded areas show the uncertainties of AGC changes estimated by 4 AGC benchmark maps.

+0.017] year^{-1}), Yunnan (+0.010 [+0.009, +0.012] Pg C year^{-1}), Guizhou (+0.010 [+0.009, +0.012] Pg C year^{-1}), and Chongqing (+0.005 [+0.005, +0.006] Pg C year^{-1}).

Spatially, the positive AGC net changes were observed for 81.65% of the area in Southwest China during 2013-2021 (Fig. 5A), with the AGC sinks able to be observed in Sichuan, northern Chongqing, Guizhou, and Guangxi provinces. The AGC losses, by contrast, were found in the southwestern part of the Yunnan province (Fig. 5A). Similar patterns could be observed in the yearly trend of AGC (Fig. 5B). The gross AGC losses were mainly observed in Chongqing, eastern Guizhou, western Guangxi, and Yunnan provinces (Fig. 5D). In parallel, areas with high gross AGC gains (Fig. 5C) correspond to areas of gross AGC sink, offsetting these AGC losses and resulting in an overall net AGC increase within these areas.

For a better understanding of the negative effect of drought on the AGC dynamics, the AGC changes in 2013-2014 (2014 AGC density map minus 2013 AGC density map) and drought areas (defined as pixels with SPEI < −1 in 2013) were analyzed. In the years 2013-2014, the AGC losses (i.e., ΔAGC < 0) of −0.113 [−0.101, −0.136] Pg C year^{-1} were found over the Southwest China, with −0.107 [−0.095, −0.132] Pg C year^{-1} of the AGC losses observed from drought-affected areas (Fig. 6A and B), such as Yunnan and southern Sichuan provinces (Fig. 6C). In addition, the magnitude of AGC losses was related to the drought intensity (Fig. 6D), with the largest AGC losses were found in areas with SPEI < −1.5. These results suggest that the severe droughts reduced the AGC over Southwest China, leading to Southwest China transitioning to act as a net AGC loss in 2014.

Furthermore, it should be noted that more than 70% of Southwest China (especially for the Yunnan province) was also affected by severe drought during 2010-2012 (Figs. S5 and S6), which may have a legacy effect on AGC changes during the study period. Meanwhile, the precipitation and RZSM values indicated abnormally dry conditions during the period of 2013-2014 (Fig. S3B), providing unfavorable growing conditions for vegetation over Southwest China.

AGC dynamics for each land use type

The influence of ecological projects on AGC over Southwest China during 2013-2021 was quantified (Fig. 7), indicated by the net AGC changes for each land use type. Overall, the net AGC changes in all land use types were positive during 2013-2021 (Fig. 7A). Nonforests exhibited the largest AGC sink (+0.032 [+0.028, +0.036] Pg C year^{-1}; Fig. 7A), followed by the persistent forests

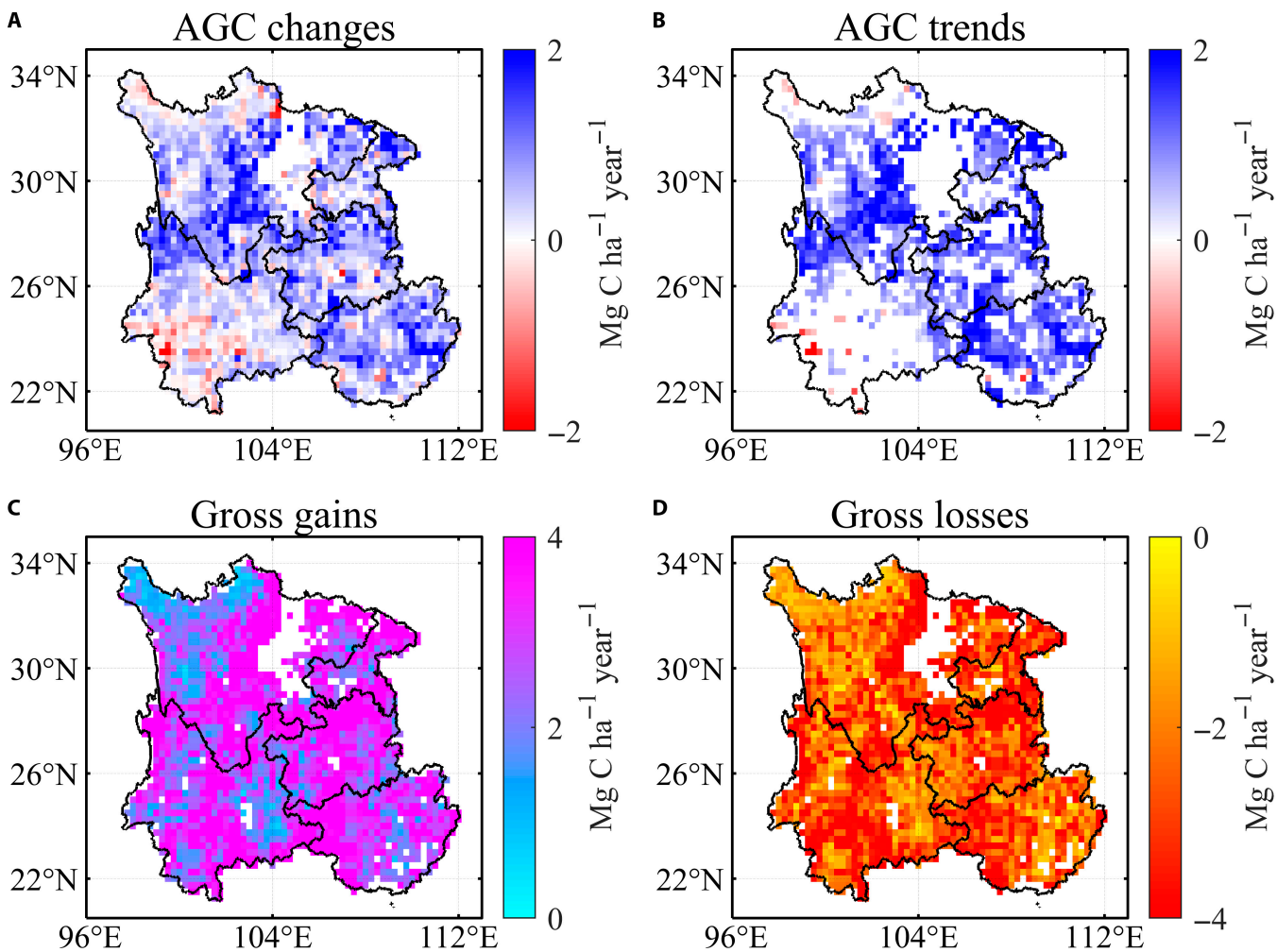

Fig. 5. Spatial patterns of AGC density changes during 2013-2021. (A) Yearly net changes, (B) trends, (C) gross gains, and (D) gross losses in AGC density during the 2013-2021 period. Yearly AGC trends are indicated by significantly positive (blue) and negative (red) trends (linear trend; $P < 0.1$). Gross AGC gains and gross AGC losses were calculated, respectively, by aggregating positive and negative AGC changes, for consecutive years during 2013-2021.

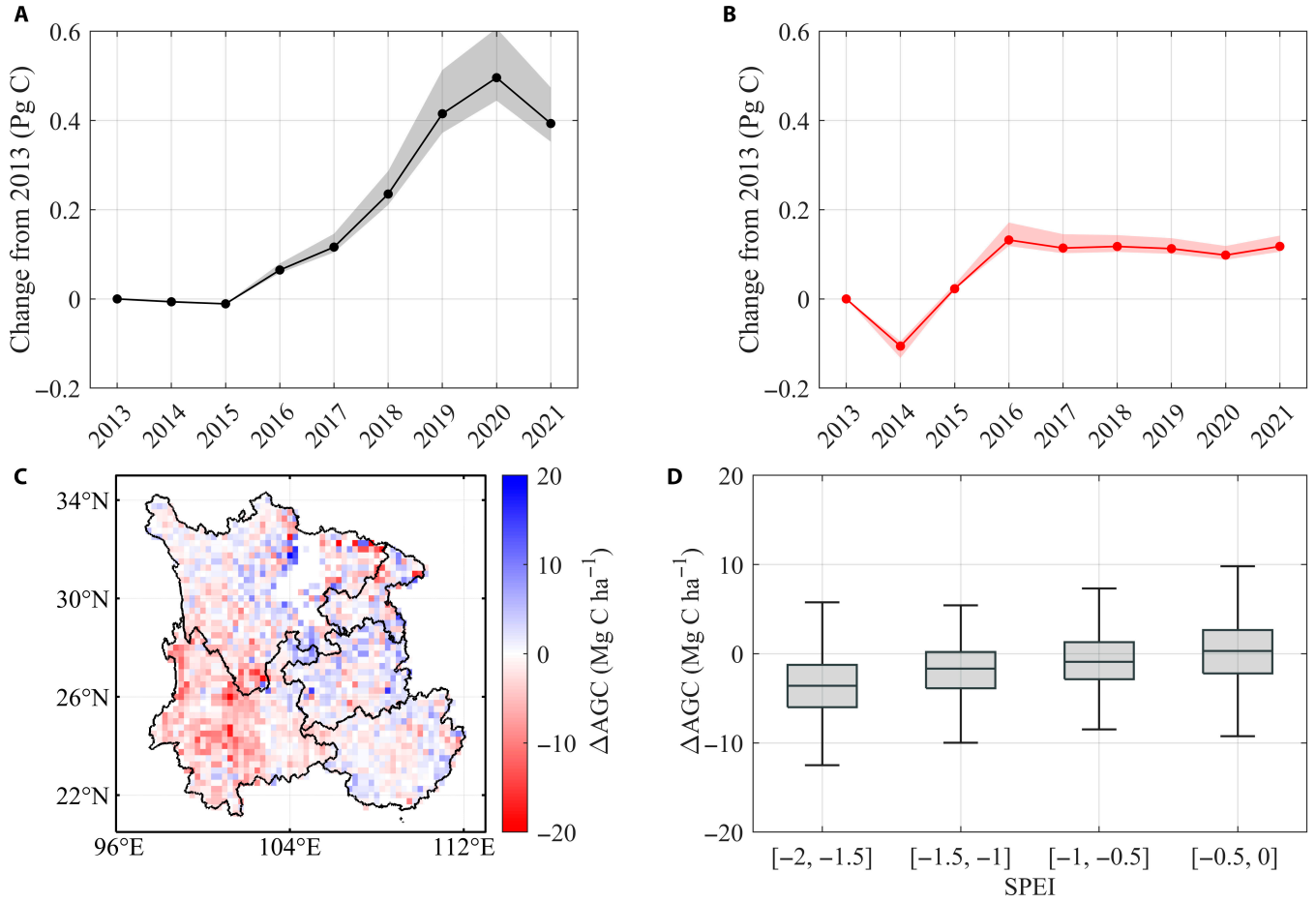

Fig. 6. Yearly net AGC changes from 2013 over the nondrought and drought areas. The AGC values shown were subtracted from the 2013 baseline values. (A and B) Net AGC changes for the (A) nondrought and (B) drought areas, respectively. (C) The spatial pattern of the AGC changes in 2013-2014 over Southwest China, calculated by the difference between the 2014 AGC density map and the 2013 AGC density map. (D) The relationship between the 2013-2014 AGC changes and the 2013 SPEI over Southwest China. The shaded areas in (A) and (B) show the uncertainties of AGC changes estimated by 4 AGC benchmark maps.

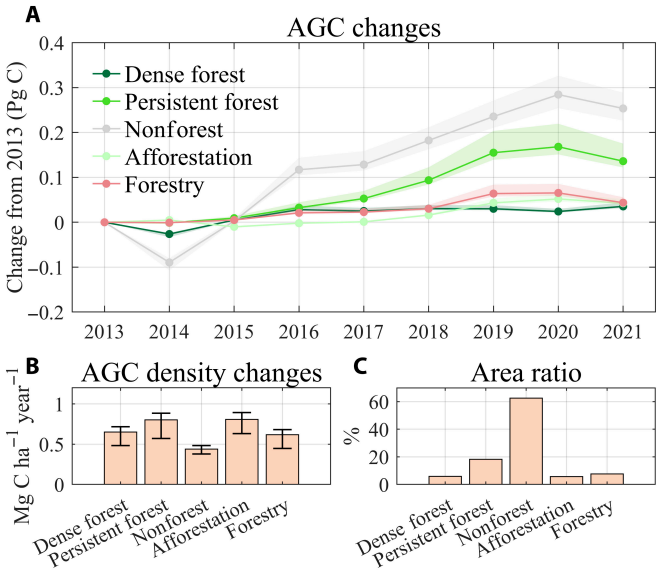

Fig. 7. Temporal dynamics of AGC for each land use type during 2013-2021. (A) AGC changes and (B) AGC density changes for each land use type. (C) Areal ratios of land use types. The shaded areas in (A) and error bars in (B) show the uncertainties of AGC changes estimated by 4 AGC benchmark maps.

(+0.017 [+0.015, +0.022] Pg C year^{-1}), afforestation (+0.005 [+0.005, +0.006] Pg C year^{-1}), forestry (+0.005 [+0.005, +0.007] Pg C year^{-1}), and dense forests (+0.004 [+0.004, +0.006] Pg C year^{-1}). The primary AGC sink in nonforests could be attributed to the large proportion (62.55%) of nonforests over Southwest China (Fig. 7C). Also, nonforests have some shrubs and small patches of trees with relatively high carbon sink capacity, which contributed to the increase in AGC over the nonforested areas of Southwest China, despite nonforests exhibited the lowest AGC density increase (Fig. 7B). Consequently, these results suggested that the nonforests dominate the AGC stock increases over Southwest China during 2013-2021.

In terms of AGC density, the afforested regions showed the largest increase in AGC density (+0.808 [+0.724, +0.985] Mg C ha^{-1} year^{-1}, Fig. 7B), suggesting that afforestation over Southwest China could be an effective way to increase the AGC density. This is, in part, likely to be the consequence of the transition from nonforests to forests as a result of tree planting. Meanwhile, a high AGC density increase of +0.803 [+0.721, +1.035] Mg C ha^{-1} year^{-1} was found in persistent forests, followed by dense forests (+0.650 [+0.583, +0.816] Mg C ha^{-1} year^{-1}), forestry (+0.619 [+0.555, +0.791] Mg C ha^{-1} year^{-1}), and nonforests (+0.438 [+0.391, +0.498] Mg C ha^{-1} year^{-1}) (Fig. 7B).

AGC dynamics in karst and nonkarst areas

Over the study period, both karst and nonkarst areas showed AGC increases (Fig. 8A). The net AGC change in karst areas was +0.022 [+0.020, +0.027] Pg C year^{-1} (29.57% of total area), nearly half of the net AGC changes in nonkarst areas (+0.042 [+0.037, +0.050] Pg C year^{-1}, 70.43% of total area) (Fig. 8A and C). Contrary to the results of AGC stock changes, karst areas have a higher AGC density increase (+0.772 [+0.692, +0.940] Mg C ha^{-1} year^{-1}) relative to nonkarst areas (+0.537 [+0.481, +0.646] Mg C ha^{-1} year^{-1}) (Fig. 8B), suggesting a high carbon sink capacity of karst areas.

We further analyzed AGC changes for each land use type of karst and nonkarst areas (Fig. 9). Over the karst areas, the AGC stock increases were mainly observed in nonforests (+0.012 [+0.010, +0.014] Pg C year^{-1}) and persistent forests (+0.005 [+0.005, +0.007] Pg C year^{-1}) (Fig. 9A). In terms of AGC density changes, the dense forests showed the largest increase in AGC density of +1.191 [+1.068, +1.468] Mg C ha^{-1} year^{-1} (Fig. 9B), followed by persistent forests (+0.842 [+0.757, +1.106] Mg C ha^{-1} year^{-1}), afforestation (+0.818 [+0.734, +1.047] Mg C ha^{-1} year^{-1}), forestry (+0.642 [+0.576, +0.816] Mg C ha^{-1} year^{-1}), and nonforests (+0.545 [+0.488, +0.637] Mg C ha^{-1} year^{-1}).

Over the nonkarst areas, the main AGC increases were also observed in nonforests (+0.020 [+0.018, +0.023] Pg C year^{-1}) as well as persistent forests (+0.012 [+0.011, +0.015] Pg C year^{-1}) (Fig. 9A). The largest AGC density increases were found in afforestation areas (+0.799 [+0.715, +0.926] Mg C ha^{-1} year^{-1}) (Fig. 9B), followed by persistent forests (+0.788 [+0.707, +1.006] Mg C ha^{-1} year^{-1}), forestry (+0.607 [+0.545, +0.779] Mg C ha^{-1} year^{-1}), dense forests (+0.576 [+0.517, +0.728] Mg C ha^{-1} year^{-1}), and nonforests (+0.393 [+0.351, +0.441] Mg C ha^{-1} year^{-1}). Generally, the nonforest areas showed the largest increase in AGC stocks in both karst and nonkarst areas during 2013-2021.

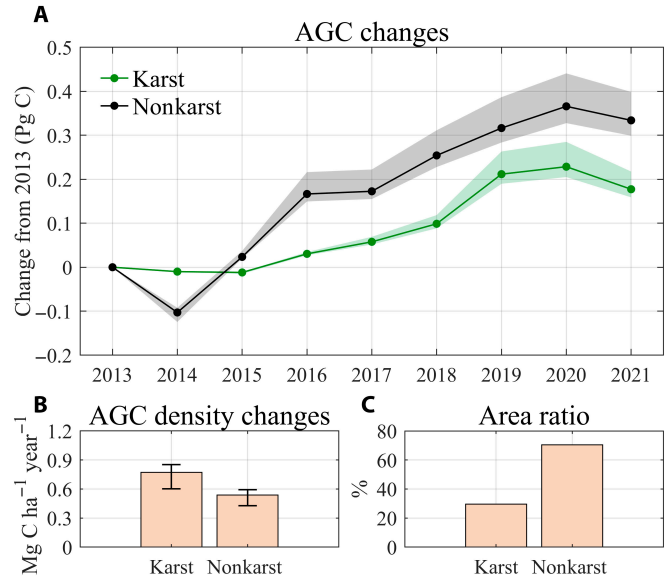

Fig. 8. AGC dynamics in karst and nonkarst areas during 2013-2021. (A) AGC changes and (B) AGC density changes in karst and nonkarst areas. (C) Area ratios of karst and nonkarst areas. The shaded areas in (A) and error bars in (B) show the uncertainties of AGC changes estimated by 4 AGC benchmark maps.

Discussion

Continuous AGC increases over Southwest China

The dynamics of AGC derived from L-VOD showed a net sink (+0.064 [+0.057, +0.077] Pg C year^{-1}) over Southwest China during 2013-2021, supporting previous findings on the increase in vegetation growth and AGC over Southwest China in recent decades [11,12,14]. The AGC increases are dominated by nonforests owing to the large areas they occupy, as reported by the study of Tong et al. [12] highlighting the high carbon uptake in nonforested areas of southern China. According to the description of Tong map [12], nonforests have several shrubs and small trees, which have a greater carbon sink capacity than herbaceous vegetation (such as grasslands and croplands). Zhang et al. [62] reported that vegetation in nonforest areas only reached 42% of the carbon sink potential, suggesting that nonforests could still absorb a large amount of CO_2 in the future. Besides, the persistent forests exhibited the large increase in AGC density over the study period, probably due to the presence of many forests with young and middle-aged trees, which still have a high carbon sink potential. Hence, maintaining the protection of persistent forests may continue to increase regional AGC stocks.

However, human disturbances associated with the reduction of vegetation cover [63] and climate change [64], such as extreme drought events, may lead to a large decrease in the AGC stocks. Our results showed that the large AGC losses during 2013-2014 were mainly occurred in the drought-affected areas, especially in the Yunnan province. After the year of 2016, persistent AGC reduction was also found in Yunnan province, suggesting that the Yunnan Province has served as a carbon loss during the period 2016-2021. The persistent AGC losses in Yunnan could be attributed to the frequent drought events that threaten the vegetation carbon sink capacity and offset the positive effect of ecological projects on AGC stocks. These results are consistent with the simulations of multiple atmospheric inversion models [7,10] that indicated a net carbon loss caused by drought over the western Yunnan Province during the period 2010-2019. Interestingly, the AGC losses in Yunnan were opposite to the greening trends indicated by LAI and NDVI values, suggesting that the recovery of AGC stocks was much slower than that of greenness after the drought perturbation. Similar results were found in the Siberian forests [33], where AGC losses and greening trends occurred simultaneously. Therefore, the protection of vegetation in Yunnan province should be enhanced by improving the effectiveness of ecological projects, to mitigate the negative impacts of drought on AGC stocks in this region.

Our estimated net AGC changes (+0.064 [+0.057, +0.077] Pg C year^{-1}) during 2013-2021 are comparable to the values (+0.050 Pg C year^{-1}) reported by Tong et al. [11] over the 2001-2012 time period. In addition, the previous estimates by Tong et al. [12] demonstrated that the AGC density increase was +0.610 Mg C ha^{-1} year^{-1}, which is close to our results (+0.655 [+0.586, +0.793] Mg C ha^{-1} year^{-1}). Our estimated net AGC changes are slightly lower than the 16-year (2002-2017) average AGC sink of +0.110 Pg C year^{-1} reported by Tong et al. [12]. This larger amount could be due to the difference in the study area extent as Tong et al. [12] considered 3 more provinces (Hubei, Hunan, and Guangdong provinces) compared to our study. Our estimated AGC stocks of 2.344 [+2.159, +2.474] Pg C in forest areas are close to the forest inventory estimates of 2.426 Pg C [65], supporting the accuracy of our AGC estimates. The small difference between our results (estimated over 2013-2021) and the forest inventory (estimated over 2009-2013) [65]

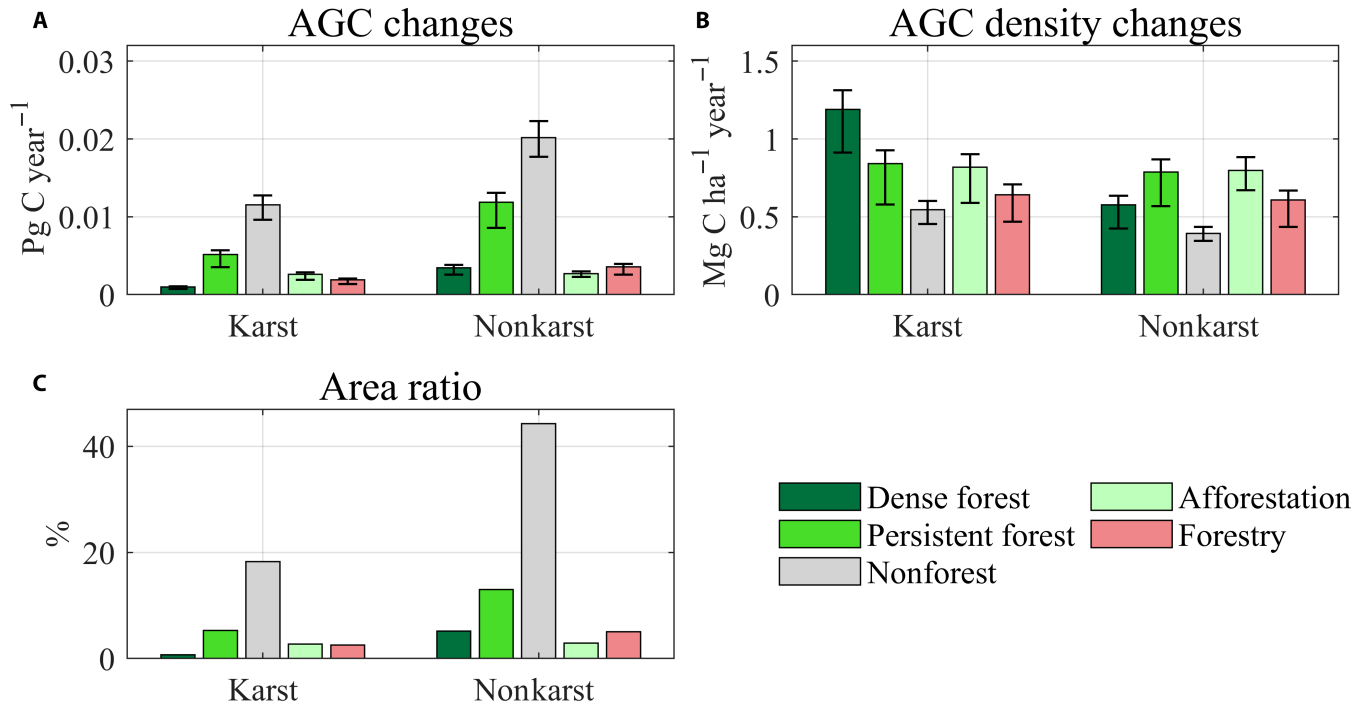

Fig. 9. Dynamics of AGC for each land use type in karst and nonkarst areas during 2013-2021. (A) AGC changes and (B) AGC density changes. (C) Areal ratios of land use types in karst and nonkarst areas. The error bars show the uncertainties of AGC changes estimated by 4 AGC benchmark maps.

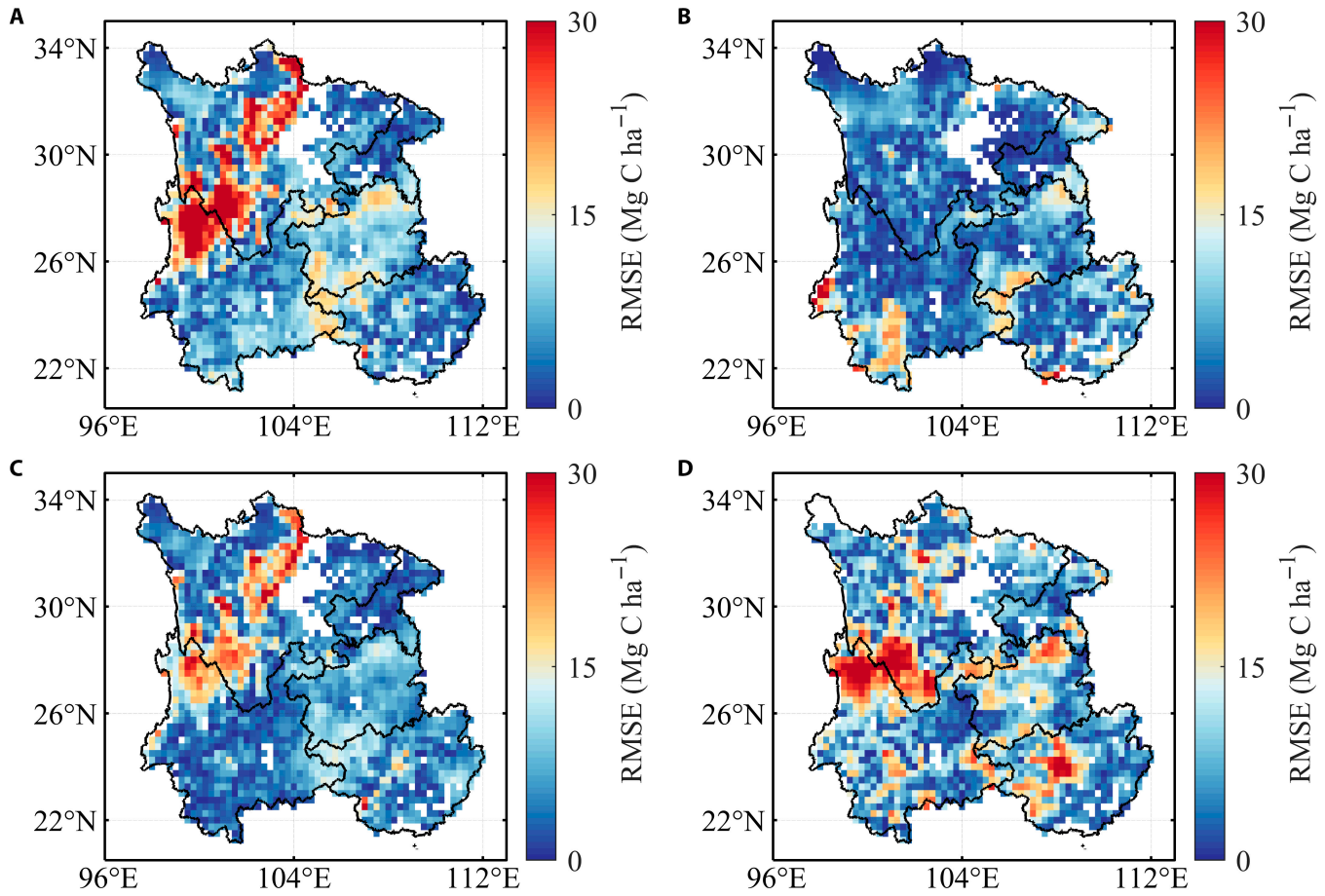

Fig. 10. Spatial patterns of the RMSE between retrieved AGC values and benchmark AGC values at the pixel scale for the year 2015, calculated using the bootstrap cross-validation method. (A) $RMSE_{Saatchi}$. (B) $RMSE_{Baccini}$. (C) $RMSE_{Saatchi\text{-}WT}$. (D) $RMSE_{Su}$.

could be attributed to the expansion of forest areas in recent decades [20,66].

Impacts of ecological projects on AGC changes

Our results showed that the afforestation areas had the largest carbon sink capacity, partly attributed to the expansion of forests in these areas. Over the past 2 decades, ecological projects in the form of afforestation have converted portions of bare ground and croplands to forests, and enforced protection intensity of existing forests over Southwest China [17,63,67]. Especially for the karst areas, the ecological conditions and forest cover rates in karst areas have improved through effective human management and protection, thus enhancing the carbon sink capacity of karst areas. Furthermore, a field-based experiment in Sichuan province [68] showed that the ecological projects reduced soil erosion and increased biodiversity by increasing the area of mixed forests, thereby mitigating the negative impact of drought on AGC stocks. Thus, the successful implementation of ecological projects and afforestation not only benefits local livelihoods but also increases AGC [15] and mitigates climate change [11].

Several studies [11,64,69] have confirmed that human management, particularly ecological restoration projects, is the predominant factor driving vegetation growth and AGC increase in Southwest China karst. In addition, Southwest China karst is mainly located in the East Asia monsoon climate zone, creating the basis for a stable and favorable climate (e.g., $Slope_{RZSM} > 0$ in Fig. S3B) during the study period [69], thereby promoting the increase of AGC over the Southwest China karst. To date, land degradation and sloping croplands still exist in karst areas [21,63], indicating that there is still a considerable carbon sink potential in these regions [70]. Addressing these issues by afforestation and tree species adjustment could increase AGC stocks in karst areas [62].

The magnitude of AGC density increase in forestry was lower than that in other forest types, despite the forestry did not belong to the scope of ecological projects [12], suggesting that the sustainable management of forests in forestry areas should be enhanced to increase the regional AGC. Forestry was mainly used as a means to alleviate poverty for local residents through timber production and fruit sales [12]. If certain forests in forestry areas no longer have the capacity to absorb CO_2 (i.e., cease to serve as a carbon sink or even transition into a carbon loss), harvesting these trees may be the best option [71]. This is because harvesting could reduce AGC losses from forest decomposition and generate wood production. Moreover, forests of native tree species could provide better performance than tree plantations on a number of ecosystem services [72], such as carbon sequestration, water provisioning, and biodiversity benefits. Restoring

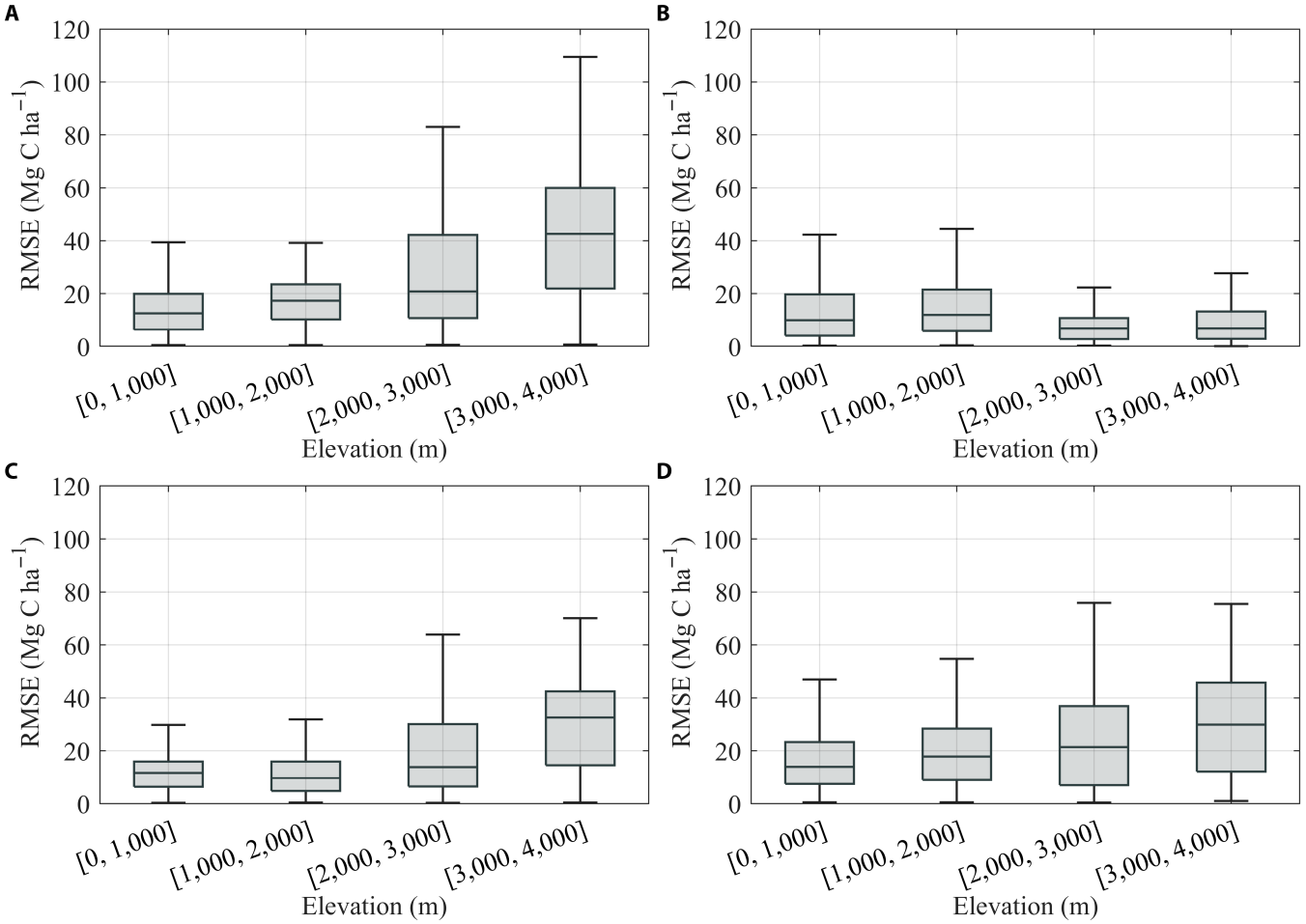

Fig. 11. The relationship between uncertainties of AGC density estimates and elevation over Southwest China. The RMSE value is calculated by 4 AGC benchmark maps, using the bootstrap cross-validation method. (A) Saatchi. (B) Baccini. (C) Saatchi-WT. (D) Su.

old plantations that are no longer intended for timber production to native forests can increase AGC stocks in forestry areas [73].

Yet, the implementation of ecological projects may generate some negative impacts on the hydrological cycle in karst areas [12]. For example, excessive afforestation may increase soil moisture consumption and evapotranspiration, leading to water shortages at local and regional scales [74]. In particular, a considerable part of plantations in Southwest China karst are *Eucalyptus*, which can consume more water than other tree species [75,76]. Extensive ecological restoration projects may also impact the local food production in Southwest China karst due to the increase of abandoned cropland [77]. The trade-off between afforestation and food provisioning and security should be given attention in future ecological restoration projects.

Uncertainties and limitations

We used 4 AGC benchmark maps (i.e., Saatchi map, Baccini map, Saatchi-WT map, and Su map) to calibrate and estimate the L-VOD-based AGC density maps during the study period. For evaluating the uncertainties associated with AGC estimates calculated for each AGC benchmark map, a bootstrap cross-validation method was used in 2015. Our results showed that the AGC stocks retrieved using the Baccini map have the highest accuracy, indicated by the lowest RMSE value of 0.153 Pg C (Table S1). At the pixel scale, the high RMSE values associated with 4 AGC benchmark maps were mainly distributed in the Hengduan Mountain and the Yunnan-Guizhou Plateau (Fig. 10), which are characterized by the complex topography and high elevations (Fig. S7). The Baccini map also exhibited lower RMSE values in AGC density estimates relative to other maps (Fig. 10B), suggesting that the Baccini map has a good performance for estimating AGC over Southwest China.

To evaluate the influence of topography on the AGC estimations over Southwest China, the relationship between uncertainties of AGC density estimates and 2 topographic factors (i.e., elevation and relief amplitude) was investigated (Figs. 11 and 12). Across 4 AGC benchmark maps, the RMSE values increased with elevation (Fig. 11), except for the Baccini map where the highest RMSE values were found at elevations between 1,000 and 2,000 m. Similarly, the RMSE values showed an upward trend with increasing relief amplitude (Fig. 12), except for the Baccini map where the highest RMSE values were observed at relief amplitude between 30 and 40 m. Thus, these results suggest that the accuracy of AGC estimates was influenced by the topographic features: higher accuracy of AGC estimates is found in areas with low elevations and flat terrain, whereas lower accuracy is found in areas with high elevations and rugged terrain.

Although a strict pre-processing method was used to filter the influence of RFI and topography, the remaining L-VOD

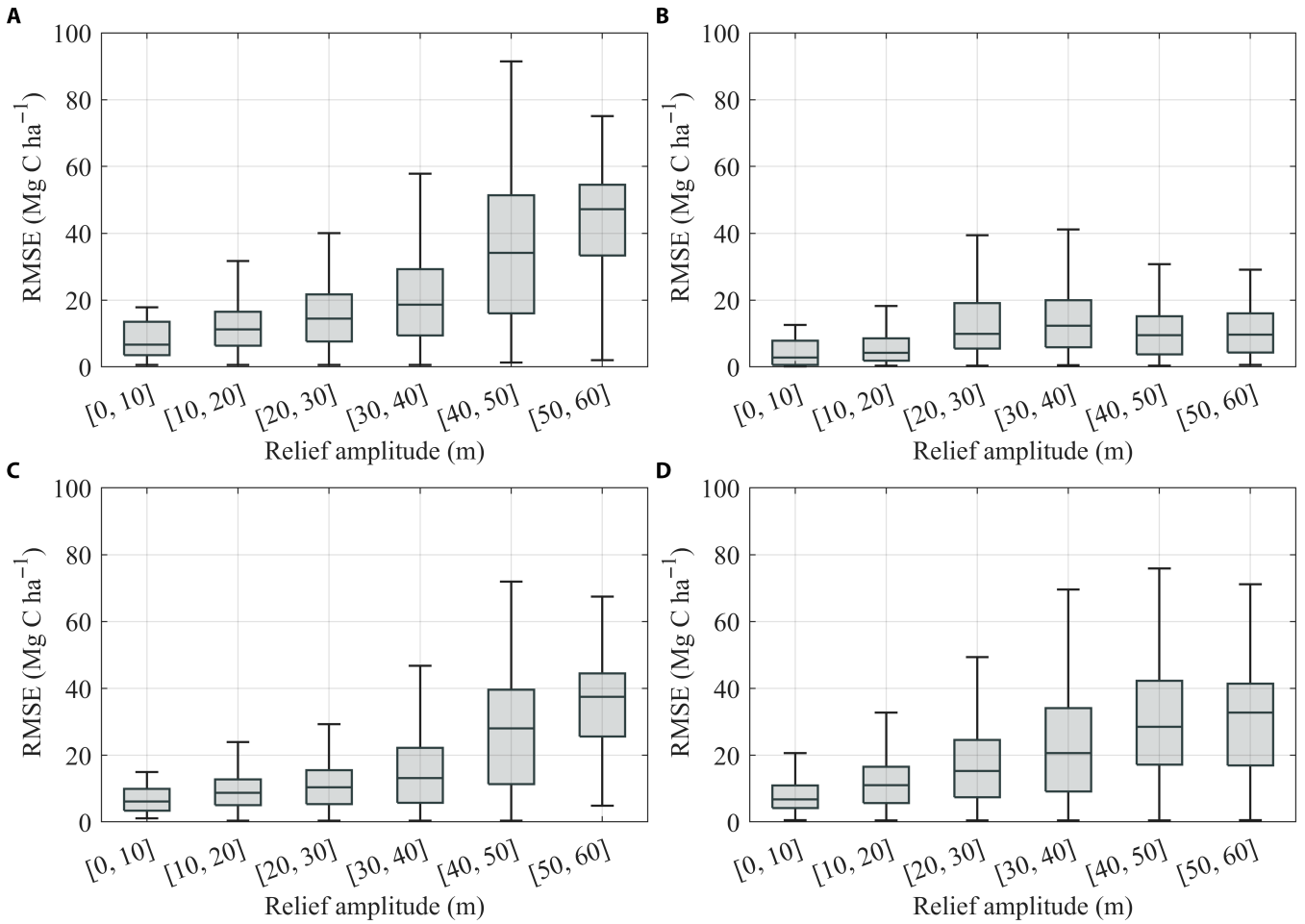

Fig. 12. The relationship between uncertainties of AGC density estimates and relief amplitude over Southwest China. The RMSE value is calculated by 4 AGC benchmark maps, using the bootstrap cross-validation method. (A) Saatchi. (B) Baccini. (C) Saatchi-WT. (D) Su.

pixels may still be affected by RFI to some extent, potentially affecting the accuracy of AGC estimation. The presence of RFI leads to the lack of L-VOD observation in a few pixels and limits the applicability of monitoring AGC dynamics in parts of Southwest China, such as the eastern part of Sichuan. Nevertheless, the negative effect of RFI on L-VOD has diminished obviously in China after 2016 [42]. Moreover, the relatively coarse spatial resolution (0.25°) of the AGC maps based on L-VOD generally limits the ability to analyze accurately the AGC dynamics for each land use type separately [32,35], because a single pixel at a resolution of 0.25° would often consist of different land use types. For example, nonforests and afforestation areas may be combined in a 0.25° grid cell, reducing our ability to accurately calculate the net AGC changes precisely at the level of classes of afforestation and nonforests.

Some uncertainties are also contained in the original Tong map, such as the uncertainty associated with the carbon density models. Additionally, the Tong map represents the land use change for the period 2002-2017, which may introduce certain uncertainties to our results.

Conclusions

In the present study, the AGC dynamics over Southwest China during 2013-2021 were analyzed using the L-VOD-derived AGC product. The AGC stocks over Southwest China exhibited a net sink of +0.064 [+0.057, +0.077] Pg C $year^{-1}$, suggesting that Southwest China represents an AGC sink over the study period. Yet, regional drought resulted in a large AGC stock decrease of −0.113 [−0.101, −0.136] Pg C $year^{-1}$ during 2013-2014, making Southwest China act as an AGC loss in 2014, especially for the Yunnan province. For each land use type, the nonforests showed the largest increase in AGC stocks (+0.032 [+0.028, +0.036] Pg C $year^{-1}$), owing to their predominance over Southwest China. For the AGC density changes, afforestation areas showed the highest increase in AGC density (+0.808 [+0.724, +0.985] Mg C ha^{-1} $year^{-1}$), suggesting that afforestation has been an effective measure for carbon sequestration over Southwest China. Given that the magnitude of AGC density increase in forestry was lower than that in other forest types, the sustainable forest management in forestry could be enhanced, in order to increase regional AGC and mitigate climate change. Furthermore, our results showed a high carbon sink capacity of the karst areas, indicated by the higher increase in AGC density of +0.772 [+0.692, +0.940] Mg C ha^{-1} $year^{-1}$ in karst areas than nonkarst areas (+0.537 [+0.481, +0.646] Mg C ha^{-1} $year^{-1}$).

Some limitations should be noted, such as the coarse spatial resolution of the AGC map, and the RFI affecting the L-VOD data over Southwest China. Additionally, the accuracy of AGC estimates is affected by topographic factors, such as elevation and relief amplitude. Further studies should use finer resolution L-VOD products to monitor AGC dynamics and utilize ancillary data to explore the drivers of AGC over Southwest China.

Acknowledgments

Funding: This study is supported in part by research grants from the National Natural Science Foundation of China (Grant Nos. 42322103, 42171339, and 41830648).
Author contributions: L.F. and G.D. designed the experiment. G.D. and L.F. conducted the analysis and wrote the manuscript. J.-P.W., R.F., F.F., Y.Y., X.X., Y.Z., S.T., L.C., Y.L., M.M., H.F., L.Y., Z.X., X.L., W.S., and X.C. revised the manuscript and provided valuable suggestions. All authors contributed to the discussion and revised the submitted manuscript.
Competing interests: The authors declare that they have no competing interests.

Data Availability

The land use map can be available from Tong et al. [12]. The MODIS LAI, NDVI, CHIRPS precipitation, ERA5 soil moisture, and topographic data are publicly available from Google Earth Engine. The SPEI data can be downloaded at https://spei.csic.es/spei_database/#map_name=spei12#map_position=1172. The karst map can be downloaded at https://www.karstdata.cn/. The L-VOD data can be available from the SMOS-IC website (https://ib.remote-sensing.inrae.fr/). The Baccini and Su AGC maps are publicly available. The Saatchi AGC map is available upon request from Dr. S. Saatchi (sasan.s.saatchi@jpl.nasa.gov). The Saatchi-WT AGC map can be available from Chang et al. [56].

Supplementary Materials

Figs. S1 to S7
Table S1

References

1. Piao S, Fang J, Ciais P, Peylin P, Huang Y, Sitch S, Wang T. The carbon balance of terrestrial ecosystems in China. *Nature*. 2009;458(7241):1009–1013.
2. Tang X, Zhao X, Bai Y, Tang Z, Wang W, Zhao Y, Wan H, Xie Z, Shi X, Wu B, et al. Carbon pools in China's terrestrial ecosystems: New estimates based on an intensive field survey. *Proc Natl Acad Sci U S A*. 2018;115(16):4021–4026.
3. Wang J, Feng L, Palmer PI, Liu Y, Fang S, Bosch H, O'Dell CW, Tang X, Yang D, Liu L, et al. Large Chinese land carbon sink estimated from atmospheric carbon dioxide data. *Nature*. 2020;586(7831):720–723.
4. Chang Z, Fan L, Wigneron J-P, Wang Y-P, Ciais P, Chave J, Fensholt R, Chen JM, Yuan W, Weimin J, et al. Estimating aboveground carbon dynamic of China using optical and microwave remote-sensing datasets from 2013 to 2019. *J Remote Sens*. 2023;3:0005.
5. Li XY, Li Y, Chen AP, Gao MD, Slette IJ, Piao SL. The impact of the 2009/2010 drought on vegetation growth and terrestrial carbon balance in Southwest China. *Agric For Meteorol*. 2019;269–270:239–248.
6. Zhang L, Xiao JF, Li J, Wang K, Lei LP, Guo HD. The 2010 spring drought reduced primary productivity in southwestern China. *Environ Res Lett*. 2012;7(4):045706.
7. He W, Jiang F, Mousong W, Weimin J, Scholze M, Chen JM, Byrne B, Liu J, Wang H, Wang J. China's terrestrial carbon sink over 2010–2015 constrained by satellite observations of atmospheric Co2 and land surface variables. *J Geophys Res Biogeosci*. 2022;127(2):e2021JG006644.
8. Byrne B, Liu J, Lee M, Baker I, Bowman KW, Deutscher NM, Feist DG, Griffith DWT, Iraci LT, Kiel M, et al. Improved constraints on northern extratropical Co2 fluxes obtained by combining surface-based and space-based atmospheric Co2 measurements. *J Geophys Res-Atmos*. 2020;125(15):e2019JD032029.

9. Liu JJ, Baskaran L, Bowman K, Schimel D, Bloom AA, Parazoo NC, Oda T, Carroll D, Menemenlis D, Joiner J, et al. Carbon monitoring system flux net biosphere exchange 2020 (Cms-flux Nbe 2020). *Earth Syst Sci Data*. 2021;13(2):299–330.
10. He W, Jiang F, Weimin J, Chevallier F, Baker DF, Wang J, Mousong W, Johnson MS, Philip S, Wang H, et al. Improved constraints on the recent terrestrial carbon sink over China by assimilating Oco-2 Xco2 retrievals. *J Geophys Res Atmos*. 2023;128(14):e2022JD037773.
11. Tong XW, Brandt M, Yue YM, Horion S, Wang KL, De Keersmaecker W, Tian F, Schurgers G, Xiao XM, Luo YQ, et al. Increased vegetation growth and carbon stock in China karst via ecological engineering. *Nat Sustain*. 2018;1(1):44–50.
12. Tong X, Brandt M, Yue Y, Ciais P, Rudbeck Jepsen M, Penuelas J, Wigneron JP, Xiao X, Song XP, Horion S, et al. Forest management in Southern China generates short term extensive carbon sequestration. *Nat Commun*. 2020;11(1):129.
13. Zhou LG, Wang XD, Wang ZY, Zhang XM, Chen C, Liu HF. The challenge of soil loss control and vegetation restoration in the karst area of southwestern China. *Int Soil Water Conserv Res*. 2020;8(1):26–34.
14. Brandt M, Yue YM, Wigneron JP, Tong XW, Tian F, Jepsen MR, Xiao XM, Verger A, Mialon A, Al-Yaari A, et al. Satellite-observed major greening and biomass increase in South China karst during recent decade. *Earth's Future*. 2018;6(7):1017–1028.
15. Erb KH, Kastner T, Plutzar C, Bais ALS, Carvalhais N, Fetzel T, Gingrich S, Haberl H, Lauk C, Niedertscheider M, et al. Unexpectedly large impact of forest management and grazing on global vegetation biomass. *Nature*. 2018;553(7686):73–76.
16. Houghton RA, Hackler JL. Sources and sinks of carbon from land-use change in China. *Glob Biogeochem Cycles*. 2003;17(2):1034.
17. Delang CO, Zhen Y. *China's Grain for Green program*. Switzerland: Springer International Publishing; 2015. Chapter 1, China's reforestation and rural development programs; p. 19–35.
18. Fang J, Yu G, Liu L, Hu S, Chapin FS 3rd. Climate change, human impacts, and carbon sequestration in China. *Proc Natl Acad Sci U S A*. 2018;115(16):4015–4020.
19. Liu J, Li S, Ouyang Z, Tam C, Chen X. Ecological and socioeconomic effects of China's policies for ecosystem services. *Proc Natl Acad Sci U S A*. 2008;105(28):9477–9482.
20. Lu F, Hu H, Sun W, Zhu J, Liu G, Zhou W, Zhang Q, Shi P, Liu X, Wu X, et al. Effects of national ecological restoration projects on carbon sequestration in China from 2001 to 2010. *Proc Natl Acad Sci U S A*. 2018;115(16):4039–4044.
21. Yue YM, Qi XK, Wang KL, Liao CJ, Tong XW, Brandt M, Liu B. Large scale rocky desertification reversal in South China karst. *Prog Phys Geogr-Earth Environ*. 2022;46(5):661–675.
22. Huang W, Ho HC, Peng YY, Li L. Qualitative risk assessment of soil erosion for karst landforms in Chahe town, Southwest China: A hazard index approach. *Catena*. 2016;144:184–193.
23. Barrachina M, Cristobal J, Tulla AF. Estimating above-ground biomass on mountain meadows and pastures through remote sensing. *Int J Appl Earth Obs Geoinf*. 2015;38:184–192.
24. He B, Li X, Quan X, Qiu S. Estimating the aboveground dry biomass of grass by assimilation of retrieved Lai into a crop growth model. *IEEE J Sel Top Appl Earth Obs*. 2014;8(2):550–561.
25. Zheng G, Chen JM, Tian QJ, Ju WM, Xia XQ. Combining remote sensing imagery and forest age inventory for biomass mapping. *J Environ Manag*. 2007;85(3):616–623.
26. Myneni RB, Keeling CD, Tucker CJ, Asrar G, Nemani RR. Increased plant growth in the northern high latitudes from 1981 to 1991. *Nature*. 1997;386(6626):698–702.
27. Zeng YL, Hao DL, Huete A, Dechant B, Berry J, Chen JM, Joiner J, Frankenberg C, Bond-Lamberty B, Ryu Y, et al. Optical vegetation indices for monitoring terrestrial ecosystems globally. *Nat Rev Earth Environ*. 2022;3(7):477–493.
28. Zheng XB, Kang WM, Zhao TL, Luo YX, Duan CC, Chen J. Long-term trends in sunshine duration over Yunnan-Guizhou plateau in Southwest China for 1961-2005. *Geophys Res Lett*. 2008;35(15):L15707.
29. Jin HA, Li AN, Bian JH, Nan X, Zhao W, Zhang ZJ, Yin GF. Intercomparison and validation of MODIS and GLASS leaf area index (LAI) products over mountain areas: A case study in southwestern China. *Int J Appl Earth Obs Geoinf*. 2017;55:52–67.
30. Myers-Smith IH, Kerby JT, Phoenix GK, Bjerke JW, Epstein HE, Assmann JJ, John C, Andreu-Hayles L, Angers-Blondin S, Beck PSA, et al. Complexity revealed in the greening of the Arctic. *Nat Clim Chang*. 2020;10(2):106–117.
31. Tian F, Brandt M, Liu YY, Rasmussen K, Fensholt R. Mapping gains and losses in woody vegetation across global tropical drylands. *Glob Chang Biol*. 2017;23(4):1748–1760.
32. Brandt M, Wigneron JP, Chave J, Tagesson T, Penuelas J, Ciais P, Rasmussen K, Tian F, Mbow C, Al-Yaari A, et al. Satellite passive microwaves reveal recent climate-induced carbon losses in African drylands. *Nat Ecol Evol*. 2018;2(5):827–835.
33. Fan L, Wigneron JP, Ciais P, Chave J, Brandt M, Sitch S, Yue C, Bastos A, Li X, Qin YW, et al. Siberian carbon sink reduced by forest disturbances. *Nat Geosci*. 2022;16:56–62.
34. Qin YW, Xiao XM, Wigneron JP, Ciais P, Brandt M, Fan L, Li XJ, Crowell S, Wu XC, Doughty R, et al. Carbon loss from forest degradation exceeds that from deforestation in the Brazilian Amazon. *Nat Clim Chang*. 2021;11(5):442–448.
35. Fan L, Wigneron JP, Ciais P, Chave J, Brandt M, Fensholt R, Saatchi SS, Bastos A, Al-Yaari A, Hufkens K, et al. Satellite-observed pantropical carbon dynamics. *Nat Plants*. 2019;5(9):944–951.
36. Wigneron JP, Fan L, Ciais P, Bastos A, Brandt M, Chave J, Saatchi S, Baccini A, Fensholt R. Tropical forests did not recover from the strong 2015-2016 El Nino event. *Sci Adv*. 2020;6(6):eaay4603.
37. Liu YY, van Dijk AIJM, de Jeu RAM, Canadell JG, McCabe MF, Evans JP, Wang G. recent reversal in loss of global terrestrial biomass. *Nat Clim Chang*. 2015;5(5):470–474.
38. Konings AG, Piles M, Das N, Entekhabi D. L-band vegetation optical depth and effective scattering albedo estimation from Smap. *Remote Sens Environ*. 2017;198:460–470.
39. Ma B, Jing J, Liu B, Xu Y, Dou S, He H. Quantitative assessment of the relative contributions of climate change and human activities to NPP changes in the southwest karst area of China. *Environ Sci Pollut Res Int*. 2022;29(53):80597–80611.
40. Dong G, Fan L, Fensholt R, Frappart F, Ciais P, Xiao X, Sitch S, Xing Z, Ling Y, Zhou Z, et al. Asymmetric response of primary productivity to precipitation anomalies in Southwest China. *Agric For Meteorol*. 2023;331:109350.
41. Zhang CH, Qi XK, Wang KL, Zhang MY, Yue YM. The application of geospatial techniques in monitoring karst

vegetation recovery in Southwest China: A review. *Prog Phys Geogr-Earth Environ*. 2017;41(4):450–477.
42. Wigneron JP, Li XJ, Frappart F, Fan L, Al-Yaari A, De Lannoy G, Liu XZ, Wang MJ, Le Masson E, Moisy C. SMOS-IC data record of soil moisture and L-VOD: Historical development, applications and perspectives. *Remote Sens Environ*. 2021;254:112238.
43. Oliva R, Daganzo E, Kerr YH, Mecklenburg S, Nieto S, Richaume P, Gruhier C. SMOS radio frequency interference scenario: Status and actions taken to improve the RFI environment in the 1400–1427-Mhz passive band. *IEEE Trans Geosci Remote Sens*. 2012;50(5):1427–1439.
44. Myneni R, Knyazikhin Y, Park T. MODIS/Terra leaf area index/Fpar 8-day L4 global 500m SIN grid V061. Nasa Eosdis Land Processes Daac. 2021. [accessed 1 Dec 2022]. https://doi.org/10.5067/Modis/Mod15a2h.061
45. Didan K, Modis T. Vegetation indices 16-day L3 global 1km SIN grid V061. Nasa Eosdis Land Processes Daac. 2021. [accessed 1 Dec 2022]. https://doi.org/10.5067/Modis/Mod13a2.061
46. Funk C, Peterson P, Landsfeld M, Pedreros D, Verdin J, Shukla S, Husak G, Rowland J, Harrison L, Hoell A, et al. The climate hazards infrared precipitation with stations--A new environmental record for monitoring extremes. *Sci Data*. 2015;2:150066.
47. Hersbach H, Bell B, Berrisford P, Biavati G, Horányi A, Muñoz Sabater J, Nicolas J, Peubey C, Radu R, Rozum I, et al. Era5 monthly averaged data on single levels from 1959 to present. Copernicus Climate Change Service (C3s) Climate Data Store (Cds). 2019. [accessed 2 Dec 2022] https://doi.org/10.24381/cds.f17050d7
48. Song L, Li Y, Ren Y, Xiuchen W, Guo B, Tang X, Shi W, Ma M, Han X, Zhao L. Divergent vegetation responses to extreme spring and summer droughts in southwestern China. *Agric For Meteorol*. 2019;279:107703.
49. Xing ZP, Fan L, Zhao L, De Lannoy G, Frappart F, Peng J, Li XJ, Zeng JY, Al-Yaari A, Yang K, et al. A first assessment of satellite and reanalysis estimates of surface and root-zone soil moisture over the permafrost region of Qinghai-Tibet plateau. *Remote Sens Environ*. 2021;265:112666.
50. Vicente-Serrano SM, Begueria S, Lopez-Moreno JI. A multiscalar drought index sensitive to global warming: The standardized precipitation evapotranspiration index. *J Clim*. 2010;23(7):1696–1718.
51. Liu C, Yang C, Yang Q, Wang J. Spatiotemporal drought analysis by the standardized precipitation index (SPI) and standardized precipitation evapotranspiration index (SPEI) in Sichuan Province, China. *Sci Rep*. 2021;11(1):1280.
52. Cui T, Fan L, Ciais P, Fensholt R, Frappart F, Sitch S, Chave J, Chang Z, Li X. First assessment of optical and microwave remotely sensed vegetation proxies in monitoring aboveground carbon in tropical Asia. *Remote Sens Environ*. 2023;293:113619.
53. Farr TG, Rosen PA, Caro E, Crippen R, Duren R, Hensley S, Kobrick M, Paller M, Rodriguez E, Roth L, et al. The shuttle radar topography Mission. *Rev Geophys*. 2007;45(2):RG2004.
54. Saatchi SS, Harris NL, Brown S, Lefsky M, Mitchard ET, Salas W, Zutta BR, Buermann W, Lewis SL, Hagen S, et al. Benchmark map of forest carbon stocks in tropical regions across three continents. *Proc Natl Acad Sci U S A*. 2011;108(24):9899–9904.
55. Baccini A, Goetz SJ, Walker WS, Laporte NT, Sun M, Sulla-Menashe D, Hackler J, Beck PSA, Dubayah R, Friedl MA, et al. Estimated carbon dioxide emissions from tropical deforestation improved by carbon-density maps. *Nat Clim Chang*. 2012;2(3):182–185.
56. Chang ZB, Hobeichi S, Wang YP, Tang XL, Abramowitz G, Chen Y, Cao NN, Yu MX, Huang HB, Zhou GY, et al. New forest aboveground biomass maps of China integrating multiple datasets. *Remote Sens*. 2021;13(15):2892.
57. Su YJ, Guo QH, Xue BL, Hu TY, Alvarez O, Tao SL, Fang JY. Spatial distribution of forest aboveground biomass in China: Estimation through combination of spaceborne lidar, optical imagery, and forest inventory data. *Remote Sens Environ*. 2016;173:187–199.
58. Santoro M, Cartus O, Carvalhais N, Rozendaal DMA, Avitabile V, Araza A, de Bruin S, Herold M, Quegan S, Rodriguez-Veiga P, et al. The global forest above-ground biomass pool for 2010 estimated from high-resolution satellite observations. *Earth Syst Sci Data*. 2021;13 (8):3927 –3950.
59. Huang HB, Liu CX, Wang XY, Zhou XL, Gong P. Integration of multi-resource remotely sensed data and allometric models for Forest aboveground biomass estimation in China. *Remote Sens Environ*. 2019;221:225–234.
60. Liu JY, Kuang WH, Zhang ZX, Xu XL, Qin YW, Ning J, Zhou WC, Zhang SW, Li RD, Yan CZ, et al. Spatiotemporal characteristics, patterns, and causes of land-use changes in China since the late 1980s. *J Geogr Sci*. 2014;24(2):195–210.
61. Chen C, Park T, Wang X, Piao S, Xu B, Chaturvedi RK, Fuchs R, Brovkin V, Ciais P, Fensholt R, et al. China and India lead in greening of the world through land-use management. *Nat Sust*. 2019;2(2):122–129.
62. Zhang XM, Brandt M, Yue YM, Tong XW, Wang KL, Fensholt R. The carbon sink potential of southern China after two decades of afforestation. *Earth Future*. 2022;10(12):e2022EF002674.
63. Yue YM, Liao CJ, Tong XW, Wu ZB, Fensholt R, Prishchepov A, Jepsen MR, Wang KL, Brandt M. Large scale reforestation of farmlands on Sloping Hills in South China karst. *Landsc Ecol*. 2020;35(6):1445–1458.
64. Wu LH, Wang SJ, Bai XY, Tian YC, Luo GJ, Wang JF, Li Q, Chen F, Deng YH, Yang YJ, et al. Climate change weakens the positive effect of human activities on karst vegetation productivity restoration in southern China. *Ecol Indic*. 2020;115:106392.
65. Zhao MM, Yang JL, Zhao N, Liu Y, Wang YF, Wilson JP, Yue TX. Estimation of China's forest stand biomass carbon sequestration based on the continuous biomass expansion factor model and seven forest inventories from 1977 to 2013. *For Ecol Manag*. 448(2019):528–534.
66. Chen X, Chen TX, Yan QY, Cai JT, Guo RJ, Gao MN, Wei XQ, Zhou SJ, Li CF, Xie Y. The ongoing greening in Southwest China despite severe droughts and drying trends. *Remote Sens*. 2021;13(17):3374.
67. Zhai D-L, Jian-Chu X, Dai Z-C, Cannon CH, Grumbine RE. Increasing tree cover while losing diverse natural forests in tropical Hainan, China. *Reg Environ Chang*. 2013;14(2):611–621.
68. Hua F, Wang X, Zheng X, Fisher B, Wang L, Zhu J, Tang Y, Yu DW, Wilcove DS. Opportunities for biodiversity gains under the world's largest reforestation programme. *Nat Commun*. 2016;7:12717.
69. Zhang X, Yue Y, Tong X, Wang K, Qi X, Deng C, Brandt M. Eco-engineering controls vegetation trends in Southwest China karst. *Sci Total Environ*. 2021;770:145160.
70. Jiang X, Ziegler AD, Liang S, Wang D, Zeng Z. Forest restoration potential in China: Implications for carbon capture. *J Remote Sens*. 2022;2022:0006.

71. Bellassen V, Luyssaert S. Carbon sequestration: Managing forests in uncertain times. *Nature*. 2014;506(7487):153–155.
72. Hua F, Bruijnzeel LA, Meli P, Martin PA, Zhang J, Nakagawa S, Miao X, Wang W, McEvoy C, Pena-Arancibia JL, et al. The biodiversity and ecosystem service contributions and trade-offs of forest restoration approaches. *Science*. 2022;376(6595):839–844.
73. Brown HCA, Berninger FA, Larjavaara M, Appiah M. Above-ground carbon stocks and timber value of old timber plantations, secondary and primary forests in southern Ghana. *For Ecol Manag*. 2020;472:118236.
74. Skerlep M, Steiner E, Axelsson AL, Kritzberg ES. Afforestation driving long-term surface water Browning. *Glob Chang Biol*. 2020;26(3):1390–1399.
75. Feng XM, Fu BJ, Piao S, Wang SH, Ciais P, Zeng ZZ, Lu YH, Zeng Y, Li Y, Jiang XH, et al. Revegetation in China's loess plateau is approaching sustainable water resource limits. *Nat Clim Chang*. 2016;6(11):1019–1022.
76. Jackson RB, Jobbagy EG, Avissar R, Roy SB, Barrett DJ, Cook CW, Farley KA, le Maitre DC, McCarl BA, Murray BC. Trading water for carbon with biological carbon sequestration. *Science*. 2005;310 (5756):1944 –1947.
77. Qiu S, Peng J, Quine TA, Green SM, Liu H, Liu Y, Hartley IP, Meersmans J. Unraveling trade-offs among reforestation, urbanization, and food security in the South China karst region: How can a hinterland province achieve SDGs? *Earth Future*. 2022;10(12):e2022EF002867.